Unraveling compensation between electron transfer and strain in Ni-Ag-MoS<inf>2</inf> photocatalyst

(article starts on next page)

Unraveling compensation between electron transfer and strain in Ni-Ag-MoS$_2$ photocatalyst

Ekta Rani [a,*], Vandna K. Gupta [b], Md Thasfiquzzaman [a], Parisa Talebi [a], Anna Martinelli [b], Yuran Niu [c], Alexei Zakharov [c], Marko Huttula [a], Minna Patanen [a], Harishchandra Singh [a], Wei Cao [a]

[a] Nano and Molecular Systems Research Unit, Faculty of Science, University of Oulu, FIN-90014, Finland
[b] Department of Chemistry and Chemical Engineering, Chalmers University of Technology, 412 96 Gothenburg, Sweden
[c] MAX IV Laboratory, Lund University, Lund 22484, Sweden

ARTICLE INFO

ABSTRACT

Despite the boom in catalytic response *via* constructing interfaces, understanding interfaces' interaction in heterostructures is still a paradox. In this work, the interaction of Ni with MoS$_2$ in Ni-Ag-MoS$_2$ heterostructure are unveiled through synchrotron X-PEEM and what's more, the missing interaction mechanism at the Ag-MoS$_2$ interface is probed *via* Raman mapping. The observed competition between the downshift of the E$_{2g}^1$ and A$_{1g}$ modes due to charge carrier injection and the upshift of the E$_{2g}^1$ and A$_{1g}$ modes due to compressive strain during reverse laser power experiment is assigned to the non-uniform growth of Ag nanoparticles, their intimate contact with MoS$_2$, and Ag intercalated layered MoS$_2$. The substantial improvement of the H$_2$ yield of the Ni-Ag-MoS$_2$ ($\sim$55 μmol h^{-1} g^{-1}) over the pristine MoS$_2$ and the binary Ag-MoS$_2$ evidence successful bonding of Ni, Ag and MoS$_2$. This study highlights the importance of considering both electronic coupling and strain to optically tune electromechanical properties of MoS$_2$.

1. Introduction

Photocatalysts, projected as one of the most promising catalytic media of producing H$_2$, are key for the development of sustainable energy sources to achieve the goal of averting imminent climate change while sustaining economic growth. The typically used industrial photocatalysts, such as TiO$_2$, or carbon nitrides are active at ultraviolet wavelengths constituting < 5 % of the solar spectrum. Unfortunately, practical strategies often fall short for binary/ternary photocatalysts due to under-explored various interfacial interactions. Two-dimensional (2D) transition metal dichalcogenides, such as MoS$_2$, have recently attracted attention for environmental-friendly applications [1]. However, bulk MoS$_2$ is known to be less efficient for hydrogen evolution reaction (HER) due to photocatalytically inactive basal plane of MoS$_2$, as only the extremely active sulfur terminated edges display robust nature, and slightly more positive conduction band position relative to the redox potential of H$^+$/H$_2$ [2]. Nevertheless, the physical properties of MoS$_2$ can substantially be modulated by molecular/nanoparticles (NPs) adsorption [3], applied electric field [4], and metallic contacts [5]. In the case of metal-MoS$_2$ contact, the photoactivity not only depends on layered materials' structure and properties, but also on the interface between the photocatalyst and cocatalyst [2,6]. The well-defined interface between metal and MoS$_2$ can hamper electron-hole recombination and optimize the light absorption of photocatalysts. Moreover, the physical properties MoS$_2$ can effectively be tailored through these interfaces *via* carrier injection and strain engineering [7,8]. Herein, taking the HER as an example, a combination of synchrotron and lab source-based spectro-microscopic investigations of various interfacial interactions in Ni-Ag-MoS$_2$ (MAN) ternary heterostructure is carried out.

Despite the importance, study of the interfacial contact between the layered semiconductor and hetero-junctional sites is not an easy task. As per the previous report, metallic contact between MoS$_2$ and Ni NP happens *via* Au [9] / Ag [10] nanobuffers as inferred from X-ray absorption (XA)-photoelectron emission microscopy (PEEM), referred to as X-PEEM, a spectro-microscopic full-field, synchrotron-based surface sensitive technique. The high sensitivity of the XA spectrum (XAS) to oxidization states, local structure, and electronic structure makes X-PEEM highly attractive technique. However, X-PEEM fails to probe the effect of interaction between Ag and MoS$_2$ on MoS$_2$ due to dilute concentration of Ag and technical difficulties to record XAS of Ag at the soft X-ray regions.

Raman spectroscopy, on the other hand, is an excellent local and non-destructive optical tool to probe structure and local environment in 2D materials. Furthermore, Raman mapping can monitor changes in Raman spectra at spatially different positions [11,12]. In case of metal-MoS_2 contact, Raman spectroscopy has been used to probe the effect of metal on the vibrational properties of MoS_2. Different observations, such as i) red shift in both the phonon modes due to mechanical strain induced because of metallic contact [13], ii) splitting of both E_{2g}^1 and A_{1g} modes due to biaxial strain [14], iii) splitting of E_{2g}^1 mode only due to uniaxial strain [15], and iv) shift in A_{1g} due to charge doping, whereas shift in E_{2g}^1 due to stress have been made [7,16]. In hybrid structures, dark localized surface plasmon resonances (LSPR) modes can relax non-radiatively by transferring energy to electrons *via* Landau damping leading to charge carrier (electron) injection in the lattice of the adjacent 2D semiconductor [17,18]. Till date, mainly Raman spectroscopy has been used to probe these interactions. However, this doping and strain distribution can be highly inhomogeneous, depending on the contact between the two, which mandates simultaneous microscopic and spectroscopic determinations.

In this work, we have investigated various interfacial interactions in Ni-Ag-MoS_2 (MAN) *via* X-PEEM and Raman mapping. Due to the interaction at Ag-MoS_2 interfaces, Raman spectrum of the heterosystem is dominated by compensated charge doping and compressive strain depending upon the laser power used along with intimate contact between MoS_2 and Ag. We believe that this study pushes forward the frontier of binary/ternary photocatalyst design towards efficient water splitting.

2. Experimental

2.1. Synthesis

MAN heterostructure was synthesized by utilizing a sonication based wet chemical synthesis following the method reported earlier [9]. Materials for composites include Ni nanopowder (Ningxia Orient Tantalum Industry, Co. Ltd.), MoS_2 (99.5 % assay, were purchased from Nanjing Emperor Nano Material Co. Ltd.) and $AgNO_3$ (0.01 mol/L, Sigma-Aldrich). MoS_2 powder (43.4 mg) and Ni powder (4 mg) were mixed in 100 mL de-ionized (DI) water and shaken vigorously to get evenly dispersed suspension followed by addition of $AgNO_3$ aqueous solution (1.3 mL, 0.01 mol/L) to the flask. The material synthesis was carried out by sonication using a Skymen JTS-1018 water bath ultrasonic cleaner. The cleaner was preheated to 70 °C, and the materials were then sonicated @35 kHz using maximum power ($\sim$ 3 A current) for a duration of 4 h. Post sonication, the samples were kept at room temperature overnight for the sedimentation of particles. Post sedimentation, water was carefully rinsed without losing synthesized particles, followed by decanting the synthesized particles. Drying the remaining water off from the as-prepared samples was carried out by evaporation of the water in an open beaker by utilizing a hot plate to heat samples to approximately 100 °C in the ambient air. Dried samples were then scraped off the beaker and stored in sample bottles as a dry powder. The synthesized product was then dispersed in ethanol (Sigma-Aldrich, 95.0 %) followed by drop cast on pure Si substrate. The same sample was employed for scanning electron microscopy, X-PEEM, and Raman mapping measurements. In a control experiment, Ag-MoS_2 binary system was also prepared to compare the HER of MAN with Ag-MoS_2.

It is worth noting that to reach fundamental aspects down to illustrations at electronic structural levels, the composite was synthesized and treated with the above fractions and conditions so that the compositions are well distinguished in the following spectro-microscopic studies.

2.2. Instrumentation

Zeiss Ultra plus Field emission scanning electron microscope (FESEM) was used to study the morphology of heterostructures. X-PEEM measurements on selected MAN (based on FESEM) was carried out at the AC-SPLEEM end-station of MAXPEEM Beamline at MAX IV laboratory (Lund, Sweden), using a modified SX-700 monochromator equipped with 1220.9 lines.mm^{-1} (high-density) Au/Si grating. The beamline energy resolution was estimated to be 2×10^{-4} with a photon flux of $1–5 \times 10^{12}$ ph·s^{-1} (200–900 eV range). The photon energy was scanned across Ni L$_{2,3}$ edge with a 0.2 eV step. More details regarding the PEEM measurements can be found in a previous study [19].

Micro-Raman mapping measurements were performed in backscattering geometry at room temperature using an InVia Raman spectrophotometer from Renishaw equipped with an air cooled charged coupled device detector. During the measurements, the confocal mode and a $\times$ 100 long working distance Leica objective with a numerical aperture (NA) of 0.75 were used. With this experimental setup, a spectral resolution of $\sim$1 cm^{-1} and a spatial resolution of about 0.8 μm (approximating to the relation 1.22·λ/ NA, where λ is the wavelength of the incoming laser) could be achieved. The mapping measurements were performed with different values of the laser power varying it from 0.5 to 10 % of the source power (100 mW). The Raman data was collected with 532 nm laser excitation. Before the measurement, the spectrophotometer was calibrated to the first-order vibrational mode of a Si wafer centered at 520.3 cm^{-1}.

2.3. Photocatalytic reduction of water for H_2 evolution

The catalytic activity of the pristine and synthesized heterostructure was carried out in a photoreactor to measure any activity differences. Pristine MoS_2, Ag decorated MoS_2 and MAN heterostructure were used to run experiments in the same conditions, such as identical cells, same volume, an equal amount of DI-water, a total weight of 5 mg of each sample, and fixed illumination time of 2 h. A magnetic stirring bar for stirring the suspension was always present during the experiment. The 5 mg samples were added into a quartz bottle with a total volume of 68 mL. For each experiment, 3 s sonication was carried out to provide a consistent starting point in terms of the dispersion of the suspension. The gaseous content was flushed for a fixed repeatable starting point by using argon. In the first round of preparation, we applied careful Ar-flushing, including heating of the water, to minimize the water-dissolved air. The argon flush's primary function was to establish a reliable control method to monitor gas leaks that arose through effusion and, to a lesser extent, diffusion mechanisms, thus detecting potential abnormally high leak rates. By utilizing the available monochromatic wavelengths each at the time, eight experiments per sample were carried out. The repetitive nature of the experiments also provided initial results of the reusability of the samples.

For HER measurements, samples were cycled in Perfect Light PCX50B photo reactor through eight monochromatic LED light sources covering near UV regime to visible light (in a range of 365 to 630 nm) equipped with magnetic stirring. Sampling and analysis of gaseous species were carried out using Agilent Micro 490 GC gas chromatograph equipped with an H_2 sensitive column (10MS5A) after the end of each illumination round.

3. Results

Pristine MoS_2, Ag decorated MoS_2 and MAN heterostructure were used to run HER experiments and it was found that MAN sys-

tem is superior to the pristine MoS₂ and Ag decorated MoS₂. Thus, MAN is further investigated by employing spectro-microscopic techniques. In MAN, the MoS₂ sheets and Ni NP are bonded *via* Ag NPs. The diameter of the Ag NPs is found to be ∼20 nm, whereas the diameter of Ni NPs is ∼100 nm.

3.1. One to one SEM, X-PEEM and Raman mapping

The SEM image of MAN is shown in Fig. 1a. Fig. 1b shows the X-PEEM image while the corresponding XAS spectrum is shown in Fig. 1d. By tuning the synchrotron beam energy from 845 to 875 eV, the XAS covered the main features of Ni $L_{2,3}$ edges. The main peaks in the Ni 2p XAS are associated with the Ni $2p_{3/2,1/2} \rightarrow$ 3d dipole transitions, separated by spin–orbit splitting of 17.3 eV. The general spectral line shape in the MAN displays similar features to Ni metal foil, suggesting the stability of Ni NPs during the wet chemical synthesis. For the XAS spectra collected from MAN, a small peak turns out at the photon energy of 861 eV. However, its rather weak intensity leaves questions to deduce its origin, e.g., satellite feature of the Ni^0, or Ni atoms bonded with S atoms of MoS₂, as observed in nickel chalcogenide nanofilms [20]. Even in the latter case, the rather low intensity compared with the main peak show that the bonded Ni atoms are rather few in comparison to that of the Ni-Au-MoS₂ system [9]. Nevertheless, a rather low charge transfer between the Ni NPs and the flat MoS₂ basal plane beneath and the protruding layer is possible. The metal particle is thus connected to the semiconductor through basal and side contacts. Although X-PEEM uncovers the interaction between MoS₂ and Ni, the interaction between Ag and MoS₂ and its effect on MoS₂ cannot be explored using the same. For this reason, we employed lab source-based Raman mapping.

Fig. 1c shows the Raman image of MAN at the same location (as that for SEM and X-PEEM) and corresponding Raman spectra are plotted at various spatial position within MAN (Fig. 1e). Raman

spectra of MAN exhibits mainly-two phonon modes, E_{2g}^1 and A_{1g}. Along with these two modes, E_{1g} mode at ∼286 cm⁻¹ and higher intensity of out-of-plane A_{1g} are noted. According to the Raman selection rules, the E_{1g} mode is forbidden in backscattering experiment on the basal plane of bulk MoS₂ [21]. However, when the incident light scatters on the surface of edge terminated MoS₂, the corresponding scattering Raman tensor undergoes a rotation transformation, leading to a nonzero differential scattering cross-section and hence the E_{1g} mode can be observed indicating film formation of MoS₂. Moreover, the peak intensity of the out-of-plane A_{1g} mode is like that of the in-plane E_{2g}^1 mode in the bulk MoS₂ and 3 times that of the E_{2g}^1 mode in the MoS₂ film. Such preferred excitation of an out-of-plane mode is also consistent with the vertical-aligned crystal texture of the film sample considering the polarization dependence of the Raman scattering cross-section. When measured at spatially different positions, Raman measurements of MAN show variation in the Raman spectra, such as red shift in the phonon frequency of E_{2g}^1 and A_{1g} modes compared to pristine MoS₂ (Fig. 1c & e). The observed variation of optical phonons is further investigated using power dependent Raman mapping to probe the effect of Ag NPs on MoS₂.

3.2. Power dependent Raman mapping

Many sets of power dependent (0.5, 1, 5, and 10 %) Raman mapping are collected on various sites to make appropriate observations. At a low laser power (0.5 %), no variation could be seen as E_{2g}^1 and A_{1g} modes are observed consistently at ∼384 and 409 cm⁻¹, which is similar to pristine MoS₂. However, when the same region is excited with higher laser power (1, 5 and 10 %), variation in phonon frequency is noted. Representative Raman images for different regions are shown in Figs. 2 & 3 and Fig. S1. All the peak positions are obtained by fitting Raman spectra with Lorentzian line shape (Fig. S2 and Table S1/S2).
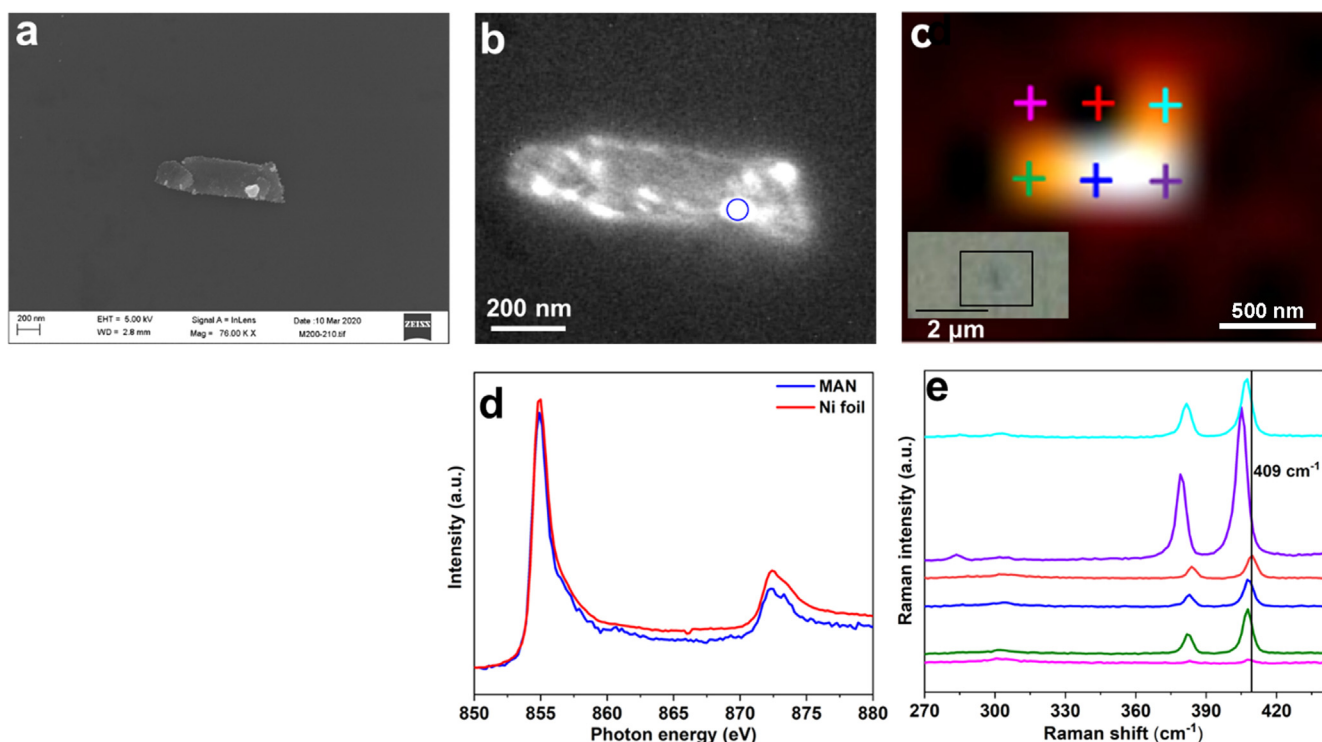

Fig. 1. (a) SEM image, (b) X-PEEM image, (c) Raman image created using phonon frequency 370–420 cm⁻¹, corresponding (d) XAS spectrum of MAN along with XAS spectrum of Ni foil, and (e) Raman spectra at various locations marked in the Raman image (Fig. 1c). Inset of Fig. 1c show the optical image of MAN.
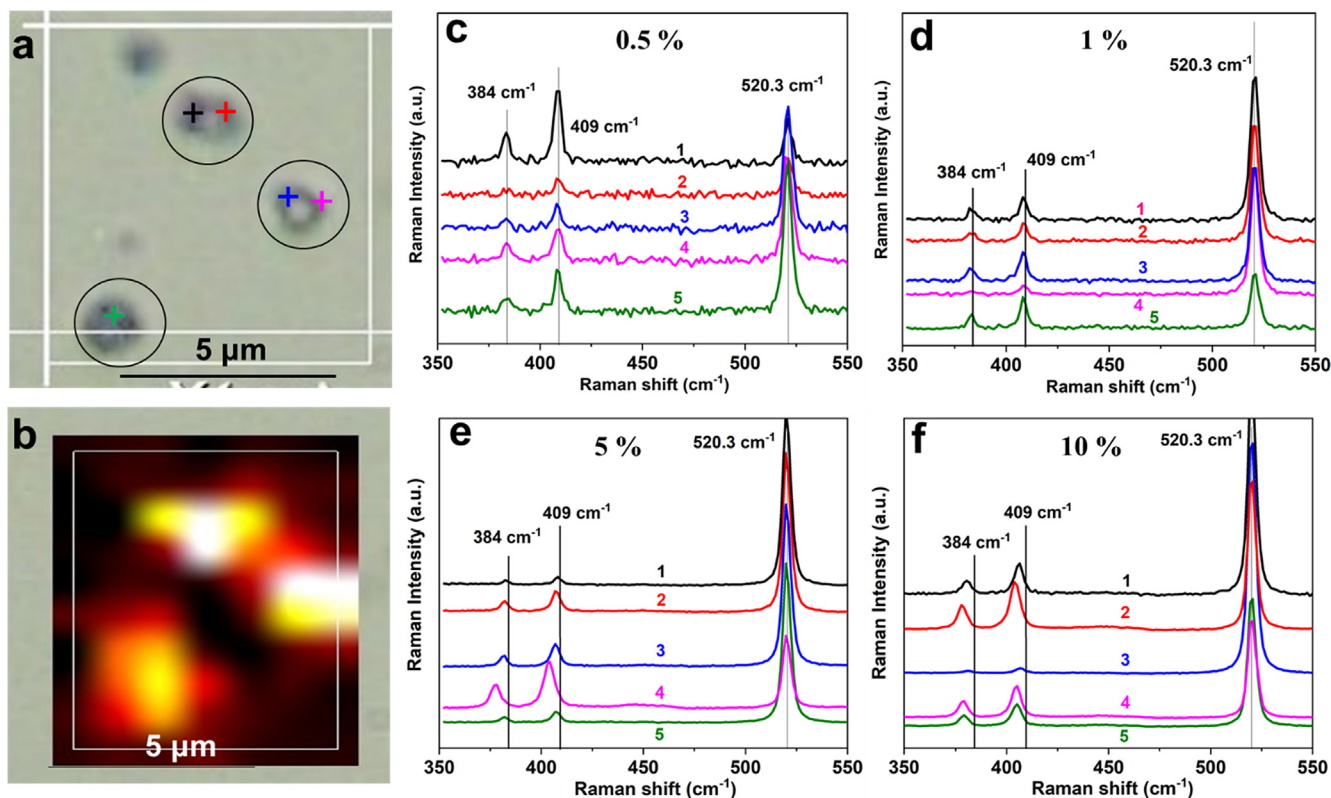
Fig. 2. (a) Optical image, (b) Raman image created using phonon frequency 370–420 cm^{-1}, corresponding Raman spectra collected at 0.5 (c), 1 (d), 5 (e), and 10 % (f) laser power at various location as marked in the optical image (a).

Increase in the laser power from 0.5 to 1 % led to either no change or slight red shift in both E_{2g}^1 and A_{1g} modes (Fig. 4). Enhanced red shift in both E_{2g}^1 and A_{1g} modes is further observed with the increase in laser power to 5 %. However, further increment in laser power led to both red and blue shift in E_{2g}^1 and A_{1g} modes at different locations (Fig. 4 & Fig. S1f). Comparison of different Raman mapping data collected at four different laser power shows that increase in the laser power led to red shift as well as blue shift in E_{2g}^1 and A_{1g} modes at spatially different locations. Moreover, one can see that both E_{2g}^1 and A_{1g} modes follows the same pattern with the change in the laser power.

As a further analysis, Fig. S3 shows the average phonon frequency for both the A_{1g} and the E_{2g}^1 mode, including all the 13 points investigated in Fig. 3. Fig. S3 reveals that, on average, the laser power leads to red shift in the frequencies (note that the vibrational mode of Si maintains a constant value and is hence used as our internal reference). The slightly larger errors visible for higher power of 5 and 10 % are a direct consequence of the more spread values found while investigating the different spots. The observed spatial variation could be ascribed to i) laser heating, ii) mechanical strain induced due to presence of Ag NPs, and iii) interplay between charge injection and stress.

Vasa et al. [16] have reported Raman spectra of MoS$_2$ as a function of excitation power in the range from 0.69 and 21.84 mW. No appreciable peak shift as a function of laser power was noted for either of the two modes. This suggests that MoS$_2$ is quite stable with respect to laser power and observed changes here cannot possibly arise due to increase laser power. Moreover, laser heating give rise to uniform red shift in the phonon frequency and increment in red shift due to increased laser power. However, here we have observed both red and blue shift in E_{2g}^1 and A_{1g} modes at different laser powers. Moreover, different phonon frequencies are

observed at spatially different location. Thus, the effect of laser heating can be negated.

Observed changes in the Raman spectra could be due to local mechanical strain due to metal-MoS$_2$ contact [14,15,22]. However, this does not seem plausible here as this strain should be laser power independent, whereas we have not observed any shift in phonon frequency at very low laser power. Moreover, as mentioned in the literature, biaxial strain leads to splits in both the E_{2g}^1 and A_{1g} modes, whereas uniaxial strain leads to splitting of mainly E_{2g}^1 mode. However, no splitting is noted here (Fig. 2 and Fig. 3). Moreover, the effects of mechanical strain in thicker MoS$_2$ layers are significantly weaker and dominantly found in monolayer or bilayer. Thus, this possibility can be negated as well.

The interplay between charge transfer and compressive stress [13,16] seems to be the most probable cause of the observed power dependent Raman shift in MAN. As per literature, A_{1g} mode corresponding to the structural distortions arising due to the out-of-plane motion of sulphur atoms on either side of Mo atoms preserves the lattice symmetry, whereas E_{2g}^1 mode corresponding to the collective in-plane motion of two layers of the sulphur atoms in the opposite direction of Mo atoms, does not preserve the lattice symmetry, hence only A_{1g} is sensitive to doping [16]. Whereas, in another work, it has been shown that charge-transfer *via* external perturbation leads to change in both the E_{2g}^1 and A_{1g} modes [13]. Herein, Fig. 4 shows that both E_{2g}^1 and A_{1g} mode follow the same trend indicating that both modes are sensitive to charge transfer and or stress. Since *n*-doping (p-doping) softens (stiffens) the modes, the observed red shift in the Raman spectra from 0.5 to 5 % suggests *n*-doping in the present case. In the current case, the electron transfer to the conduction band of MoS$_2$ can occur *via* LSPR of Ag NPs excited by the laser excitation. Since E$_{LSPR}$ >- E$_{MoS2}$ − E$_{Ag}$, the LSPRs can relax non-radiatively *via* Landau damp-
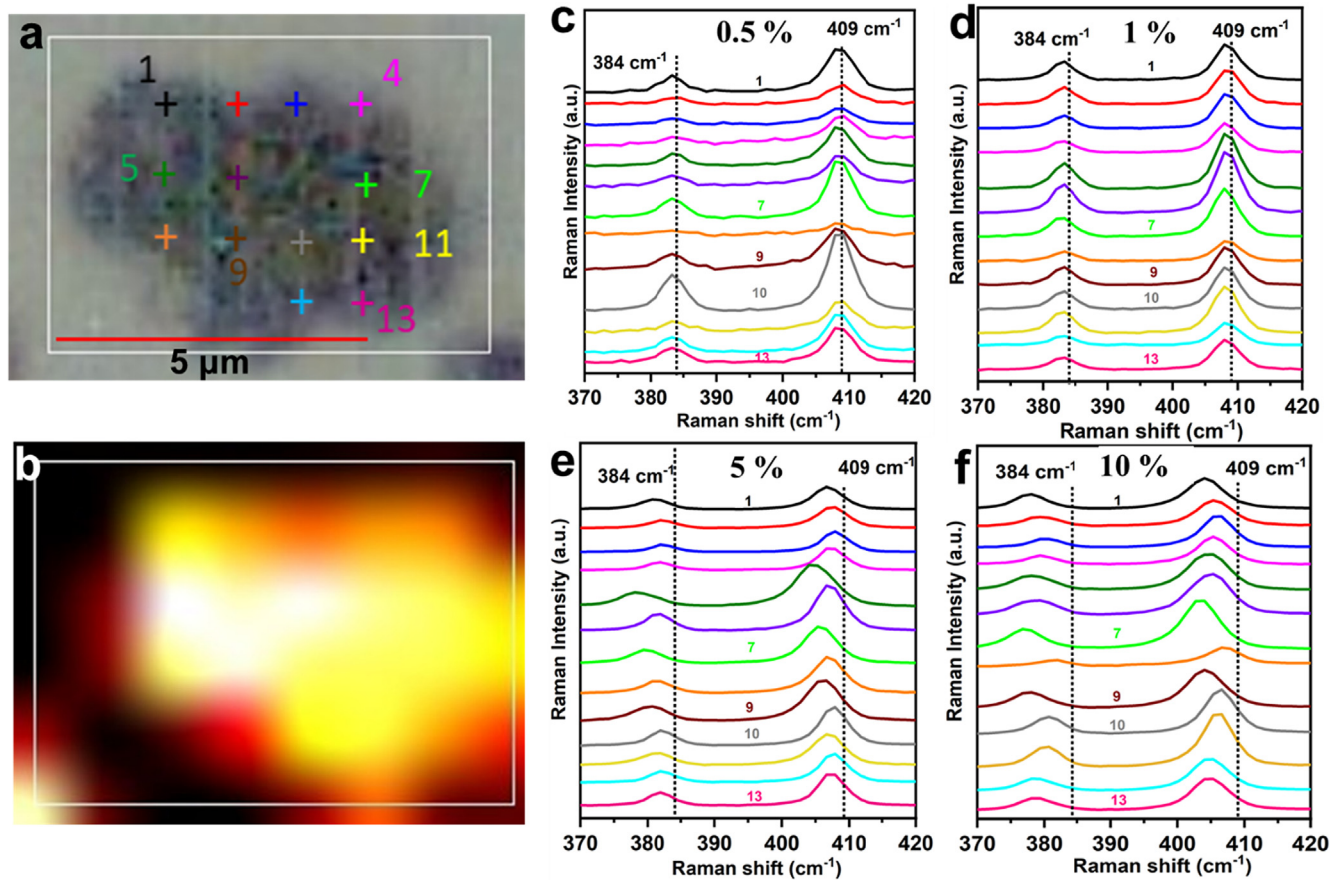
Fig. 3. (a) Optical image, (b) Raman image created using phonon frequency 370–420 cm^{-1}, corresponding Raman spectra collected at 0.5 (c), 1 (d), 5 (e), and 10 % (f) laser power at various location as marked in the optical image (a).
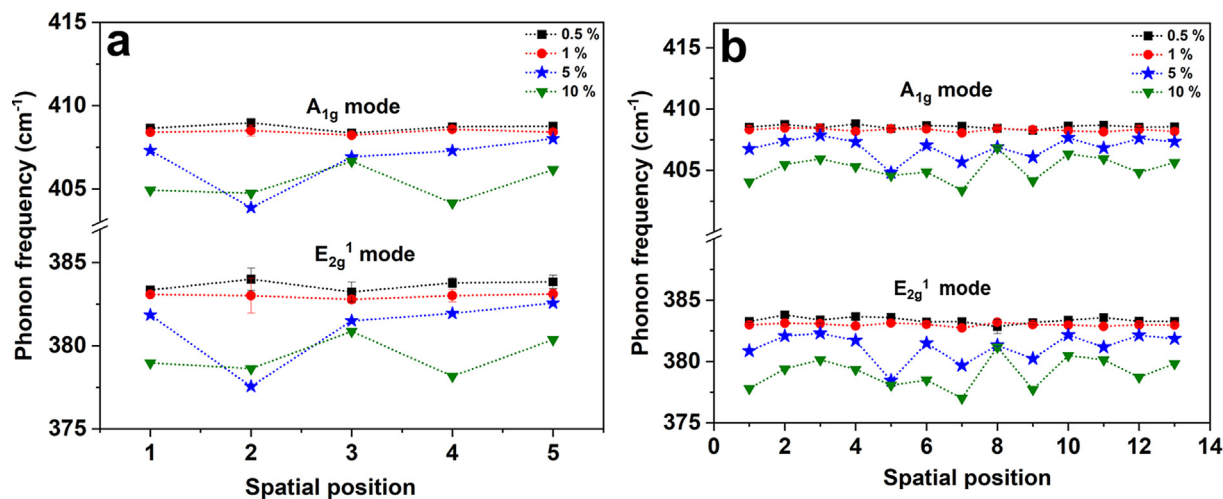

Fig. 4. Variation in phonon frequency for E$_{2g}^1$ and A$_{1g}$ modes with laser power corresponding to Fig. 2 and Fig. 3.

ing transferring the energy to free electrons in Ag. These electrons subsequently get injected into the adjacent MoS$_2$ leading to red shift in phonon modes. Moreover, laser annealing can cause compression in the MoS$_2$ leading to blue shift in the phonons at higher laser power [13].

Thus, it is inferred that power dependent laser excitation of Ag NPs in hybrid structure results in optically tunable electron transfer and compressive deformation of MoS$_2$ by electron injection *via* non-radiative relaxation of LSPRs excited in Ag NPs. The observed

shifts of two modes can be related to the extent of electron transfer concentration and strain and by the relations given as follows [13],

$$\omega_i = k_n(i)n \tag{1}$$

$$\Delta\omega = -2\gamma_i\omega_i^0\gamma\varepsilon_i \tag{2}$$

Equations (1) and (2) enable the calculation of Raman peak frequencies for constant carrier concentration and strain. Here, ε is the lattice strain, n is the charge carrier concentration, γ_i is the

Grüneisen parameter corresponding to phonon frequency ω_i, ω_i^0 is the phonon frequency of unstrained and undoped MoS$_2$, and k_n is -0.33 cm^{-1} per 10^{13} cm^{-2} e$^-$ and -2.22 cm^{-1} per 10^{13} cm^{-2} e$^-$ for E$_{2g}^1$ and A$_{1g}$ mode [13], respectively. Average room temperature γ value is 0.86 and 0.15 for E$_{2g}^1$ and A$_{1g}$ mode, respectively. Since the observed phonon frequencies at 0.5 % laser excitation is same as that of pristine MoS$_2$, we have chosen E$_{2g}^1 \sim 384$ cm^{-1} (ω_1^0) and A$_{1g} \sim 409$ cm^{-1} (ω_2^0) as the undoped and unstrained value. The inferred laser power dependence of electron transfer concentration and the associated strain averaged over the laser spot size is noted in Table 1 & Table 2. The electron density as well as strain are different at different spatial locations, even though Raman mapping was collected at same laser power.

Observed difference in Raman spectrum at different spatial locations can be ascribed to various possible reasons, such as i) non-uniform growth of Ag NPs, ii) larger size of laser spot (0.8 μm) compared to Ag NPs (10–20 nm) and iii) intercalation of Ag in MoS$_2$ layers. As per electron microscopy imaging, the deposition of Ag is not continuous, rather they form NPs on the surface of MoS$_2$, which can be interpreted as Volmer-Weber island growth mode [23]. Since the growth of Ag is inhomogeneous, and this inhomogeneity can give rise to two regions, one is the intimate contact between Ag clusters and MoS$_2$ surface while the other region is spaced from MoS$_2$ with a notable separation form Ag. Intimate contact between the two will give rise to larger effect of Ag NPs, whereas the effect decreases with increase in the distance between the two. Moreover, observed no changes in the Raman spectra at certain locations (Fig. 4) can be explained with reported density functional theory calculations, which predict that an interface separation of larger than 6 Å between metal and MoS$_2$ is enough to decouple MoS$_2$ from the electronic perturbation of atop metal layers [22]. This further shows that effect of Ni on the Raman spectra of MoS$_2$ can be neglected as Ni is in contact with MoS$_2$ *via* Ag NPs, thus, spaced far enough to have any effect. Since the size of laser spot is much bigger than the size of Ag NPs, laser exposure covering an area might include different number of Ag NPs, when collecting Raman data at different locations, which can give rise to varied doping concentration and strain value. The third possibility can be the intercalation of Ag between MoS$_2$ layers during the growth of Ag from AgNO$_3$. It is known that intercalation of Ag between layered structure MoS$_2$ is possible [24]. Moreover, intercalation can generate stress in the layered structures along with the possibility of charge transfer [25,26]. In the present case, as mentioned above, AgNO$_3$ is added to MoS$_2$ solution and sonicated for 4 h. Since the growth of Ag on MoS$_2$ follows the Volmer-Weber island growth mode [23], wherein nucleation followed by growth of clusters leads to isolated metal islands on MoS$_2$. The islands keep growing until a continuous and polycrystalline film forms. However, for highly mobile materials, such as Ag, the metal islands change dynamically even near room temperature, where the large islands grow at the expense of the shrinking of small islands. During this process, it can happen that smaller Ag clusters can intercalate within the MoS$_2$ layers. Growth of these clusters will depend on the separation between two adjacent layers, which is around 6 Å in the case of MoS$_2$. Thus, this intercalation can lead to varied charge doping and stress as the laser used for excitation has a depth of focus $\sim$0.66 μm, thus covering many layers of MoS$_2$. However, the intercalation of Ag within MoS$_2$ layers and its effect on electronic and vibrational properties of MoS$_2$ needs further investigation, which will be explored separately.

In order to establish the effect of laser-induced electron transfer and strain, we carried out further power dependent measurements in reverse. In this process, Raman mapping was collected at lowest laser power of 0.5 % after carrying out Raman mapping at 10 % laser power (Fig. 5 & S4). The observed reversible effect further establishes the above interpretation of electron transfer and compressive strain in MAN.

3.3. Photocatalytic H$_2$ experiment

Fig. 6a shows the measured water splitting experiment results for all the samples (bare MoS$_2$ and Ni-Ag-MoS$_2$) under white light

Table 1
Inferred electron doping concentration and the induced lattice strain as a function of laser power corresponding to Fig. 2.

Spatial location	5 %		10 %	
	Strain (%) (-ve)	Electron doping *10^{12} cm^{-2}	Strain (%) (-ve)	Electron doping *10^{12} cm^{-2}
1	0.24	3.16	0.45	11.4
2	0.28	6.53	0.79	17.2
3	0.32	7.19	0.41	8.07
4	0.89	18.5	0.73	16.1
5	0.25	6.24	0.66	14.7

Table 2
Inferred electron doping concentration and the induced lattice strain as a function of laser power corresponding to Fig. 3.

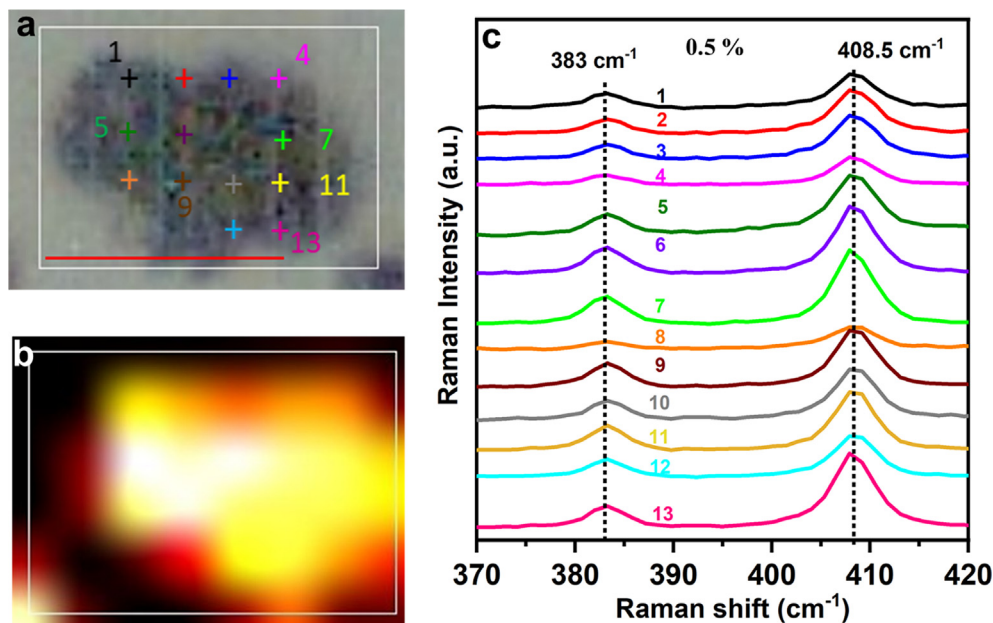| Spatial location	5 %		10 %	
	Strain (%) (-ve)	Electron doping *10^{12} cm^{-2}	Strain (%) (-ve)	Electron doping *10^{12} cm^{-2}
1	0.44	7.73	0.85	17.51
2	0.26	5.66	0.63	12.31
3	0.24	3.82	0.53	10.86
4	0.32	5.82	0.64	13.05
5	0.76	14.60	0.82	15–38
6	0.34	6.88	0.76	14.40
7	0.60	11.72	0.96	19.98
8	0.36	7.42	0.39	7.61
9	0.52	10.29	0.86	17.08
10	0.26	4.62	0.48	9.31
11	0.39	7.61	0.53	10.86
12	0.26	4.88	0.72	14.72
13	0.29	5.84	0.57	11.93

Fig. 5. (a) Optical image, (b) Raman image created using phonon frequency 370–420 cm^{-1}, corresponding Raman spectra collected at 0.5 % laser power after carrying out Raman mapping at higher laser power as shown in Fig. 3.
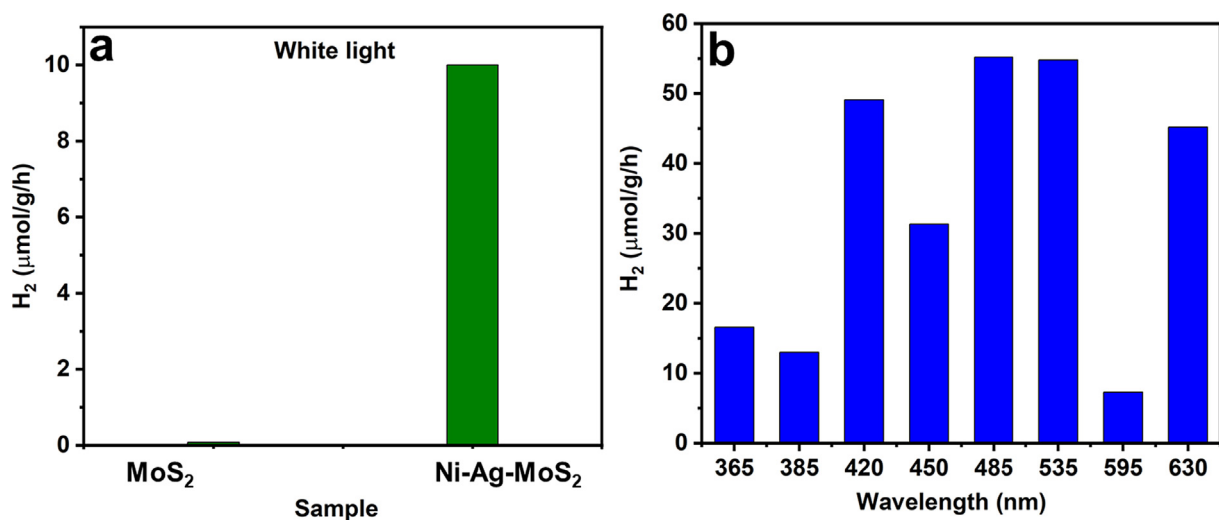

Fig. 6. Hydrogen yield (a) for different samples at white light and (b) for MAN at different wavelengths in the range of 420–630 nm.

illumination. Bare MoS$_2$ show negligible H$_2$ yield, whereas MAN shows significant H$_2$ production. Based on the white light water splitting experiment, we carried out detailed experiment in the visible to UV region for MAN. Fig. 6b shows the H$_2$ production rate of MAN in the light range of 365 nm to 630 nm. As can be seen from Fig. 6b, at the excitation wavelength of 485 and 535 nm, the observed HER performance for MAN is ∼55 μmol g^{-1}h^{-1}. The observed lesser HER at 595 nm could be due to experimental error.

A cyclic test on the MAN system was carried out for 3 cycles with each cycle of 2 h under white light irradiation. An Agilent 8860 GC was employed to quantify the evolved H$_2$. The catalyst was stably functional in HER as shown in Fig. S5 of the Supplementary material. The SEM was performed on MAN sample after the cycling tests. Depicted in Fig. S6a, the Ni NPs were firmly attached on to the MoS$_2$ through side and basal contacts. The metals of Ni

and Ag coexist with these of S and Mo from the semiconductor matrix according to the element mapping of Fig. S6b. A high-resolution transmission electron microscopic evaluation (HRTEM) was further performed on the sample after the cyclic tests. Both the Ni NPs and flakes are well retained in the composite in Fig. S7(a). The selected area electron diffraction (SAED) pattern further proved that the main crystal structures of MoS$_2$ and Ni were kept in Fig. S7(b) and (c). From the above microscopic and microstructural studies, samples are stable after 3 cycles of photocatalysis. The control experiment by using the Ag-MoS$_2$ was also performed and < 2 μmol/g/h HER yield was found when using the white light as the incident source. Thus, the MAN system is superior to the bare MoS$_2$ and binary Ag-MoS$_2$ systems within the photocatalytic HER abilities. It's worth noting HER is mainly investigated here and the full water splitting requires dedicated

instrumental setups and calibrations along with spectro-microscopic investigations of OER reactive sites to deduce mechanisms. However, a recent work of the similar system [10] showed the oxygen evolution is accompanied with the HER, denoting a full water splitting capability of the MAN system. Beside the same composites, the fraction of Ni used here falls into the range of the MAN system studied previously. Thus, full water splitting capability is also expected on the present sample.

4. Discussion

The possibility to not only probe locally, but visualize a chemical structure, composition, conformational state, and effect of various components on heterostructures and its catalytic activity has stimulated the development of imaging techniques. Both the spectro-microscopic techniques used here are fingerprint, rich, non-destructive and give information of different interactions (Fig. 7). MoS_2 being a cheap and abundant mineral has promising applications in transistors, optoelectronics, and UV–vis light convertors. Furthermore, it has photocatalytic abilities in degrading organic pollutants. Despite these achievements, the MoS_2 is a poor photocatalysts. However, the chemical robustness could be enhanced by heterostructure engineering. Herein, Ni-Ag-MoS_2 contact is established using facile wet chemical synthesis method. Lab-based Raman mapping and synchrotron-based X-PEEM verified the successful bonding of Ni to the layered MoS_2 at the nanoscale interface regions via the Ag buffer (Fig. 7). Moreover, power dependent Raman mapping showed the same pattern of downshift or upshift in the phonon frequency of E_{2g}^1 and A_{1g} modes with the increase in laser power due to various possibilities, such as non-uniform growth of Ag NPs, the contact between MoS_2 and Ag, larger laser spot size covering different concentration of Ag NPs, and intercalation of Ag in layered MoS_2 (Fig. 7).

A side view of ternary structure scheme is illustrated in Fig. 8a denoting metal/semiconductor contact via the MoS_2 basal and side modes. In the first mode, no biaxial strain from the dichalcogenide is needed when joining the Ni NPs onto the MoS_2 basal with the Ag as the buffer. This is supported by the absence of splits in both the E_{2g}^1 and A_{1g} of the Raman spectra in Figs. 2 and 3. In fact, the lattice of Ag (1 1 1) buffer well matches the one of the MoS_2, providing a metallic contact between the metal and semiconductor [10]. In the second case, the silver is involved in bonding the Ni NPs and the atoms at the MoS_2 edge. As a result, the M/S contact was also metallic [9] when the noble metal buffers the Ni and the MoS_2's defective side [27,28]. A band alignment scheme is depicted in Fig. 8b following the spectro-microscopic determinations. The figure adopts the work functions of 5.35 eV, 4.74 eV, and 5.20 eV for Ni, Ag and MoS_2, respectively, [10,29] and the metal–semiconductor (M/S) contact model of metal-induced gap state [30]. Therein, the interface dipole was formed by the charge transfer across the bonds at the M/S interfaces. The reference level is set to the charge neutrality level (CNL), similar to Fermi level in semiconductor itself and referring to the highest occupied surface state for the common surface [31]. Here the CNL is very close to the Ag Fermi level due to Ag's buffer status and a lower work function of the Ag than the MoS_2. As per the band alignment scheme when Ni NPs and MoS_2 are joined by Ag NPs, free electrons will transfer from Ni to MoS_2 via Ag due to the work function difference. This leads to the accumulation of electrons next to the valence band of MoS_2 adjacent to the interface region and the decrease of contact resistance which is contributing to the observed higher H_2 yield by MAN [32]. The Fermi levels of the Ni, MoS_2, and the interface region will be aligned after thermodynamic equilibrium [33], resulting in the band bending of MoS_2. During the photocatalysis, electron-hole (e^--h^+) pairs are first created on the semiconductor MoS_2 matrix. Following the aligned bands, the photoexcited electrons from the MoS_2 can thus move easily from the valence band of MoS_2 to the metal side, as shown in the Fig. 8(b). As a result, the e^--h^+ recombination is substantially inhibited [34], and a longer time window is left for the water redox than in the pure semiconductor case.
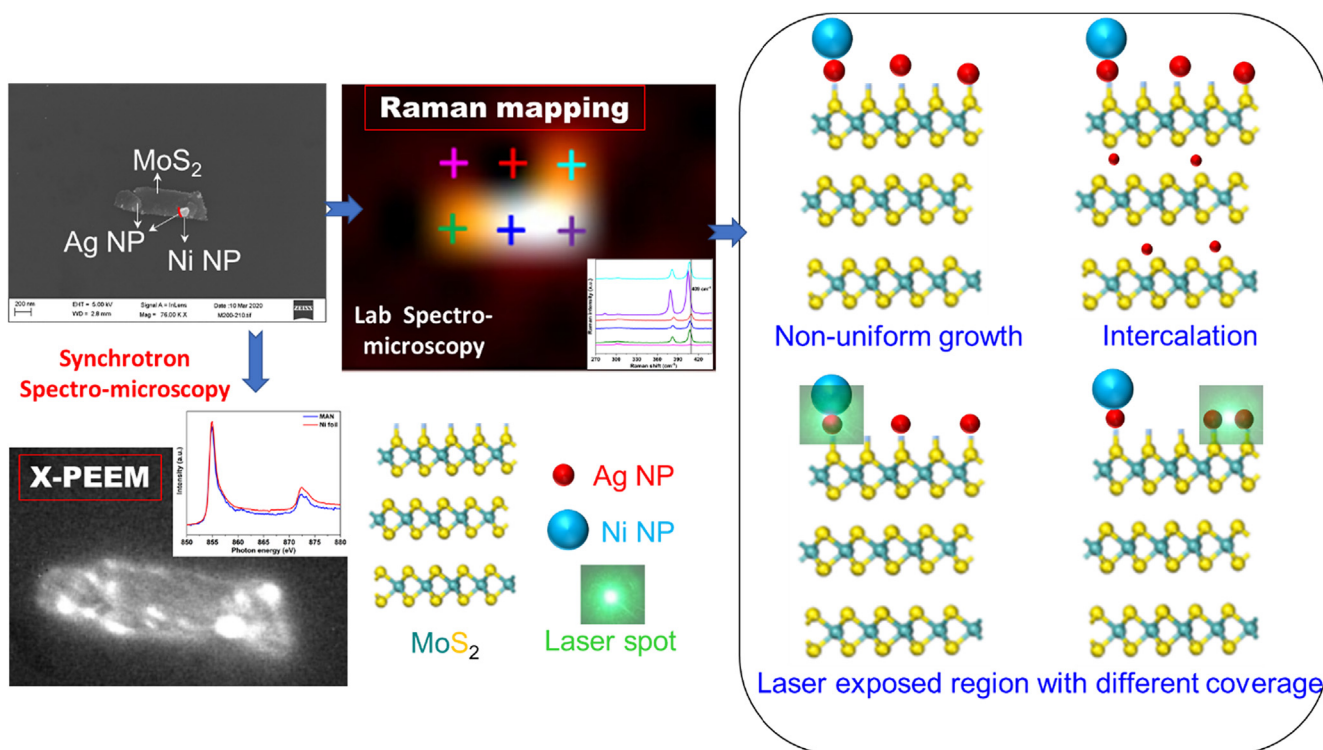

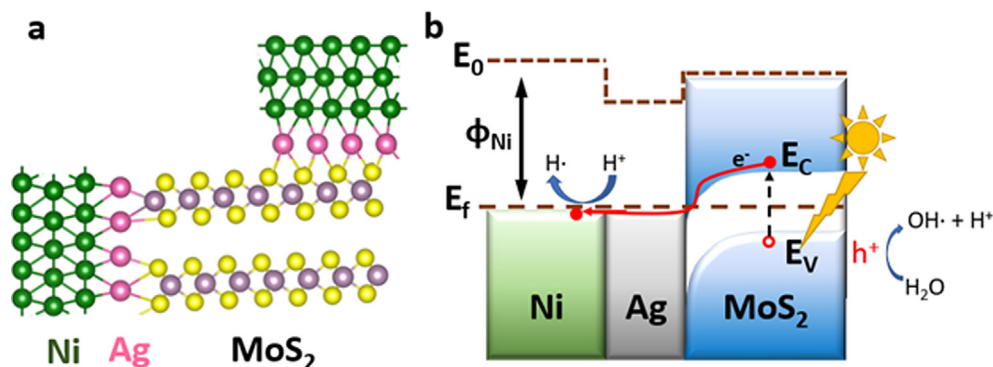**Fig. 7.** Schematic representation of lab vs synchrotron spectro-microscopy mapping studies of Ni-Ag-MoS_2.

Fig. 8. (a) Schematic of ternary structure in-side view, (b) Band alignment of the ternary interface. E_0, E_F, E_C, E_V, and Φ_{Ni}, represent the vacuum level, Fermi level of metal, the conduction and valence band of MoS_2, and the work function of Ni, respectively. Migration of photoinduced electrons is shown in red during the photocatalysis.

Holes in the MoS_2 oxide led to formations of the OH· and H^+ radicals. The protons get reduced by the electrons to form H·, and later H_2. Remaining OH· possibly combines to form the H_2O_2 or partially stack on the metal sides. In the former case, the product gets easily dissolved and emits oxygen under vigorous stirring and light irradiations. The latter one results the increase of the nickel hydroxides along with the native oxides [10] which indeed benefits the oxygen evolution reactions [35]."

5. Conclusion

Spectro-microscopic X-PEEM and Raman mappings have efficiently been used to probe Ni-Ag-MoS_2 heterostructure. The interaction of Ni with MoS_2 is evidenced through synchrotron X-PEEM, whereas the interaction mechanism at the Ag-MoS_2 interface is probed *via* Raman mapping. The large variation in E^1_{2g} and A_{1g} phonon modes in Ni-Ag-MoS_2 with the increase in laser power and pristine like behavior during reverse power dependent measurement is observed. These variations are assigned to non-uniform growth of Ag NPs and their intimate contact with MoS_2, larger laser spot size covering different concentration of Ag NPs, and Ag intercalated between layered MoS_2. These observations further reveal compensation between downshift in E^1_{2g} and A_{1g} modes due to charge carrier injection and upshift in E^1_{2g} and A_{1g} modes due to laser annealing. The improved photocatalytic activity of Ni-Ag-MoS_2 heterostructure (H_2 yield $\sim$ 55 μmol h^{-1} g^{-1}) compared to pristine MoS_2 (H_2 yield < 5 μmol h^{-1} g^{-1}) is attributed to successful bonding of Ni, Ag and MoS_2. Thus, an interesting possibility of achieving a tunability between electron injection and strain is attained by employing laser induced charge doping and stress. This LSPR-induced electron injection offers unique possibility of spatially localized dynamical electron doping and provides an active manipulation and tuning of 2D semiconductors.

Data availability

Data will be made available on request.

Declaration of Competing Interest

The authors declare that they have no known competing financial interests or personal relationships that could have appeared to influence the work reported in this paper.

Acknowledgements

Appendix A. Supplementary material

Supplementary data to this article can be found online at https://doi.org/10.1016/j.jcat.2022.09.006.

References

[1] Z. Wang, B. Mi, Environmental applications of 2D molybdenum disulfide (MoS2) nanosheets, Environ. Sci. Technol. 51 (2017) 8229–8244, https://doi.org/10.1021/acs.est.7b01466.

[2] T. Su, Q. Shao, Z. Qin, Z. Guo, Z. Wu, Role of interfaces in two-dimensional photocatalyst for water splitting, ACS Catal. 8 (2018) 2253–2276, https://doi.org/10.1021/acscatal.7b03437.

[3] M. Wang, P. Ju, W. Li, Y. Zhao, X. Han, Ag2S nanoparticle-decorated MoS2 for enhanced electrocatalytic and photoelectrocatalytic activity in water splitting, Dalt. Trans. 46 (2017) 483–490, https://doi.org/10.1039/c6dt04079a.

[4] Q. Liu, L. Li, Y. Li, Z. Gao, Z. Chen, J. Lu, Tuning electronic structure of bilayer MoS 2 by vertical electric field: a first-principles investigation, J. Phys. Chem. C. 116 (2012) 21556–21562, https://doi.org/10.1021/jp307124d.

[5] K. Schauble, D. Zakhidov, E. Yalon, S. Deshmukh, R.W. Grady, K.A. Cooley, C.J. McClellan, S. Vaziri, D. Passarello, S.E. Mohney, M.F. Toney, A.K. Sood, A. Salleo, E. Pop, Uncovering the effects of metal contacts on monolayer MoS2, ACS Nano 14 (2020) 14798–14808, https://doi.org/10.1021/acsnano.0c03515.

[6] S. Gbadamasi, M. Mohiuddin, V. Krishnamurthi, R. Verma, M.W. Khan, S. Pathak, K. Kalantar-Zadeh, N. Mahmood, Interface chemistry of two-dimensional heterostructures-fundamentals to applications, Chem. Soc. Rev. 50 (2021) 4684–4729, https://doi.org/10.1039/d0cs01070g.

[7] M. Velický, A. Rodriguez, M. Bouša, A.V. Krayev, M. Vondráček, J. Honolka, M. Ahmadi, G.E. Donnelly, F. Huang, H.D. Abruña, K.S. Novoselov, O. Frank, Strain and charge doping fingerprints of the strong interaction between monolayer MoS2and gold, J. Phys. Chem. Lett. 11 (2020) 6112–6118, https://doi.org/10.1021/acs.jpclett.0c01287.

[8] M.W. Iqbal, K. Shahzad, R. Akbar, G. Hussain, A review on Raman finger prints of doping and strain effect in TMDCs, Microelectron. Eng. 219 (2020), https://doi.org/10.1016/j.mee.2019.111152 111152.

[9] X. Shi, S. Posysaev, M. Huttula, V. Pankratov, J. Hoszowska, J.C. Dousse, F. Zeeshan, Y. Niu, A. Zakharov, T. Li, O. Miroshnichenko, M. Zhang, X. Wang, Z. Huang, S. Saukko, D.L. González, S. van Dijken, M. Alatalo, W. Cao, Metallic contact between MoS2 and Ni via Au nanoglue, Small 14 (2018) 1–10, https://doi.org/10.1002/smll.201704526.

[10] X. Shi, M. Zhang, X. Wang, A.A. Kistanov, T. Li, W. Cao, M. Huttula, Nickel nanoparticle-activated MoS 2 for efficient visible light photocatalytic hydrogen evolution, Nanoscale 14 (24) (2022) 8601–8610.

[11] E. Rani, A.A. Ingale, A. Chaturvedi, C. Kamal, D.M. Phase, M.P. Joshi, A. Chakrabarti, A. Banerjee, L.M. Kukreja, Correlation of size and oxygen bonding at the interface of Si nanocrystal in Si-SiO2 nanocomposite: a Raman mapping study, J. Raman Spectrosc. 47 (2016) 457–467, https://doi.org/10.1002/jrs.4832.

[12] E. Rani, A.A. Ingale, A. Chaturvedi, M.P. Joshi, L.M. Kukreja, Resonance Raman mapping as a tool to monitor and manipulate Si nanocrystals in Si-SiO 2 nanocomposite, Appl. Phys. Lett. 107 (2015) 1–5, https://doi.org/10.1063/1.4934664.

[13] R. Rao, A.E. Islam, S. Singh, R. Berry, R.K. Kawakami, B. Maruyama, J. Katoch, Spectroscopic evaluation of charge-transfer doping and strain in graphene/MoS2 heterostructures, Phys. Rev. B. 99 (2019), https://doi.org/10.1103/PhysRevB.99.195401 195401.

[14] J. Wu, A. Zettl, F. Wang, Probing local strain at MX 2 − metal boundaries with surface plasmon-enhanced Raman scattering, 2014.

[15] C.R. Zhu, G. Wang, B.L. Liu, X. Marie, X.F. Qiao, X. Zhang, X.X. Wu, H. Fan, P.H. Tan, T. Amand, B. Urbaszek, Strain tuning of optical emission energy and polarization in monolayer and bilayer MoS2, Phys. Rev. B - Condens. Matter Mater. Phys. 88 (2013) 1–5, https://doi.org/10.1103/PhysRevB.88.121301.

[16] G. Sharma, S.M. Rao, B.P. Singh, P. Vasa, Optically tunable charge carrier injection in monolayer MoS2, Appl. Phys. A Mater. Sci. Process. 126 (2020) 1–9, https://doi.org/10.1007/s00339-020-03839-1.

[17] M.L. Brongersma, N.J. Halas, P. Nordlander, Plasmon-induced hot carrier science and technology, Nat. Nanotechnol. 10 (2015) 25–34, https://doi.org/10.1038/nnano.2014.311.

[18] Z. Fang, Y. Wang, Z. Liu, A. Schlather, P.M. Ajayan, F.H.L. Koppens, P. Nordlander, N.J. Halas, Plasmon-induced doping of graphene, ACS Nano 6 (2012) 10222–10228, https://doi.org/10.1021/nn304028b.

[19] E. Rani, H. Singh, T. Alatarvas, M. Kharbach, W. Cao, B. Sarpi, L. Zhu, Y. Niu, A. Zakharov, T. Fabritius, M. Huttula, Uncovering temperature-tempted coordination of inclusions within ultra-high-strength-steel via in-situ spectro-microscopy, J. Mater. Res. Technol. 17 (2022) 2333–2342, https://doi.org/10.1016/j.jmrt.2022.01.170.

[20] T. Kroll, R. Kraus, R. Schönfelder, V.Y. Aristov, O.V. Molodtsova, P. Hoffmann, M. Knupfer, Transition metal phthalocyanines: insight into the electronic structure from soft x-ray spectroscopy, J. Chem. Phys. 137 (5) (2012) 054306.

[21] X. Zhang, X.F. Qiao, W. Shi, J. Bin Wu, D.S. Jiang, P.H. Tan, Phonon and Raman scattering of two-dimensional transition metal dichalcogenides from monolayer, multilayer to bulk material, Chem. Soc. Rev. 44 (2015) 2757–2785, https://doi.org/10.1039/c4cs00282b.

[22] H.J. Conley, B. Wang, J.I. Ziegler, R.F. Haglund, S.T. Pantelides, K.I. Bolotin, Bandgap engineering of strained monolayer and bilayer MoS2, Nano Lett. 13 (8) (2013) 3626–3630.

[23] J.A. Floro, S.J. Hearne, J.A. Hunter, P. Kotula, E. Chason, S.C. Seel, C.V. Thompson, The dynamic competition between stress generation and relaxation mechanisms during coalescence of Volmer-Weber thin films, J. Appl. Phys. 89 (2001) 4886–4897, https://doi.org/10.1063/1.1352563.

[24] V.M.N. Sheremetyeva, D. Niedzieslski, D. Tristant, L. Liang, L.e. Kerstetter, S.E. Mohney, Low-frequency Raman signature of Ag- intercalated few-layer MoS 2, 2D Mater. 8 (2021) 27025031.

[25] Z. Li, K. Jiang, F. Khan, A. Goswami, J. Liu, A. Passian, T. Thundat, Anomalous interfacial stress generation during sodium intercalation/extraction in MoS 2 thin-film anodes, Sci. Adv. 5 (2019) 1–9, https://doi.org/10.1126/sciadv.aav2820.

[26] I.V. Chepkasov, M. Ghorbani-Asl, Z.I. Popov, J.H. Smet, A.V. Krasheninnikov, Alkali metals inside bi-layer graphene and MoS2: insights from first-principles calculations, Nano Energy 75 (2020), https://doi.org/10.1016/j.nanoen.2020.104927 104927.

[27] Y. Shi, J.K. Huang, L. Jin, Y. Te Hsu, S.F. Yu, L.J. Li, H.Y. Yang, Selective decoration of Au nanoparticles on monolayer MoS 2 single crystals, Sci. Rep. 3 (2013) 1–7, https://doi.org/10.1038/srep01839.

[28] W. Cao, V. Pankratov, M. Huttula, X. Shi, S. Saukko, Z. Huang, M. Zhang, Gold nanoparticles on MoS2 layered crystal flakes, Mater. Chem. Phys. 158 (2015) 89–95, https://doi.org/10.1016/j.matchemphys.2015.03.041.

[29] J.H. Kim, J. Lee, J.H. Kim, C.C. Hwang, C. Lee, J.Y. Park, Work function variation of MoS2 atomic layers grown with chemical vapor deposition: the effects of thickness and the adsorption of water/oxygen molecules, Appl. Phys. Lett. 106 (2015) 10–15, https://doi.org/10.1063/1.4923202.

[30] W. Mönch, Role of virtual gap states and defects in metal-semiconductor contacts, Phys. Rev. Lett. 58 (1987) 1260–1263, https://doi.org/10.1103/PhysRevLett.58.1260.

[31] J. Robertson, New high-K materials for CMOS applications, Compr. Semicond. Sci. Technol. 1–6 (2011) 132–176, https://doi.org/10.1016/B978-0-44-453153-7.00120-6.

[32] X. Shi, S. Posysaev, M. Huttula, V. Pankratov, J. Hoszowska, J.C. Dousse, F. Zeeshan, Y. Niu, A. Zakharov, T. Li, O. Miroshnichenko, M. Zhang, X. Wang, Z. Huang, S. Saukko, D.L. González, S. van Dijken, M. Alatalo, W. Cao, Metallic contact between MoS2 and Ni via Au nanoglue, Small 14 (2018) 1704526, https://doi.org/10.1002/smll.201704526.

[33] Z. Zhang, J.T. Yates, Band bending in semiconductors: Chemical and physical consequences at surfaces and interfaces, Chem. Rev. 112 (10) (2012) 5520–5551.

[34] S. Zhu, Q. Li, F. Li, W. Cao, T. Li, One-pot synthesis of Ag+ doped BiVO4 microspheres with enhanced photocatalytic activity via a facile hydrothermal method, J. Phys. Chem. Solids. 92 (2016) 11–18, https://doi.org/10.1016/j.jpcs.2016.01.009.

[35] N. Yu, W. Cao, M. Huttula, Y. Kayser, P. Hoenicke, B. Beckhoff, F. Lai, R. Dong, H. Sun, B. Geng, Fabrication of FeNi hydroxides double-shell nanotube arrays with enhanced performance for oxygen evolution reaction, Appl. Catal. B Environ. 261 (2020) 118193.